Department of Construction Sciences
Solid Mechanics

ISRN LUTFD2/TFHF-26/5271-SE(1-36)

Stress Constrained 3D Optimization of Prestressed Concrete

Master's Dissertation by

Torsten Ohlander

Supervisor:
Mathias Wallin, Division of Solid Mechanics

Examiner:
Jonas Engqvist, Division of Solid Mechanics

Printed by Media-Tryck AB, Lund, Sweden
For information, address:
Division of Solid Mechanics, Lund University, Box 118, SE-221 00 Lund, Sweden
Webpage: www.solid.lth.se

Abstract

Concrete exhibits high compressive strength but limited tensile strength, which restricts its applications where it's structurally efficient with respect to cost, manufacturability and strength. Prestressing is commonly used to counteract tensile stress by introducing compressive forces but the combination of prestressed concrete and optimization is still under development. An important aspect is to consider material failure criteria while optimizing to achieve realistic concrete designs which are not susceptible to fatigue and cracking from too high stress.

This thesis extends an existing 3D optimization framework for prestressed concrete by introducing a stress constraint based on the Drucker-Prager yield criterion. To ensure numerical robustness, ϵ-relaxation is used to mitigate stress singularities and local stress constraints are aggregated into a single global constraint using the Kresselmeier-Steinhauser function. Numerical examples demonstrate that the stress constraint enforces the optimized designs to comply with the maximum allowable compressive and tensile strengths of the material.

Preface

This project was carried out at the Division of Solid Mechanics at Lund University during 2025 and marks the completion of my Master of Science studies in Mechanical Engineering. The work was inspired by my supervisor, prof. Mathias Wallin, whom I thank for his guidance and support throughout the project, from initial idea to completion.

Contents

1 Introduction

1.1 Background

Concrete has historically been a mixture of approximately 1 part cement, 2 parts water and 3 parts aggregate. There are many variations to each of these ingredients and ratios and can be used with additives to create concrete with different properties such as strength, density, viscosity, hardening time, thermal resistance and so forth. Since the aggregates used usually are hard rock chips and sand, concrete behaves similarly to granular materials. These granular components can bear high internal stress under compression but relies solely on the cement to resist stresses under tension. This creates an imbalance in strength with regards to compression and tension which limits the use cases where concrete is effective.

Concrete is used in structures that experience high compressive loads such as columns and foundations. Its cost, availability and mechanical properties make concrete a standard choice in building applications. Concrete also has the advantage of being a liquid before being poured on-site. Even though smaller and repetitive structures are not unusual to be pre-fabricated, most large structures are poured at the construction site. This allows for a continuous pour resulting in a unified structure without joints.

However, the casting process presents other challenges. Firstly, the concrete needs a formwork to be poured in which in many cases requires resource intensive preparations for a single use mold. On top of this, highly irregular and complex geometries may not be feasible or justifiable to cast at all [1].

Concrete production is a major contributor to global CO_2 emissions which in 2018 accounted for 1.5 Gt CO_2 [2]. A recent study showed that modern bridge constructions often use more concrete than in the past due to a combination of conservative design practices, improved construction standards and the transition from 2D paper modeling to advanced 3D computational designs [3]. Improved material efficiency can address concrete overuse leading to sustainable and cost-effective structures.

One way to improve the mechanical performance of concrete is by prestressing it. This is achieved by using steel tendons that are tensioned either before or after the concrete has hardened, resulting in pre-tensioned and post-tensioned concrete, respectively. Prestressing doesn't improve the tensile strength of the concrete itself. Instead, it offsets the tensile stresses the structure will experience in use by sacrificing some compressive strength. This is different from conventional, reinforced concrete which prevents cracking and failure by carrying tensile stresses through ductile steel reinforcements.

Structural optimization of the structure can reduce the material usage as well but has historically been problematic to use combined with concrete and cement materials due to the manufacturing challenges. This problem is further amplified with prestressed concrete since it does not only need a form specific casting mold, but also the tendon needs to be embedded with precision to be fully suspended in the concrete. Advancements have been made with regards to 3D printed concrete (3DPC) which provides a

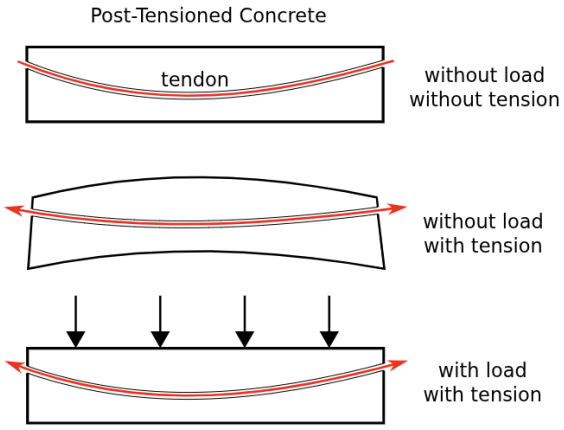

Figure 1: Simplified demonstration of a post-tensioned concrete beam. [4]

mold-free manufacturing method that enables the production of special-shape structures often generated by optimization schemes [5] [6].

This project is mostly concerned with post-tensioning due to the manufacturing difficulty in arranging a tensioned cable in a specific layout. The cable is usually fitted with anchor plates at either side of the structure to allow the cable tension to compress the whole structure which trades some fraction of the compressive strength for tensile strength.

This project is based on the work provided in [7] which presented a framework for optimizing 3D prestressed concrete structures with simultaneous topology and shape optimization. The framework allowed for optimization in 3D for complete design freedom in regards to tendon placement and variable width structures. The authors utilized the Solid Isotropic Material Penalization (SIMP) method.

This thesis aims to implement a stress constraint from the Drucker-Prager yield criterion in order to assure the final layouts and designs are realistically achievable. To facilitate this process, ϵ-relaxation is implemented together with a Kresselmeier-Steinhauser aggregation function to create a global and convex constraint to add to the original objective functions by the previously mentioned authors.

1.2 Previous Work

Optimization of concrete structures is well established, whereas the modeling of prestressed concrete within an optimization framework is more recent. Early studies mainly focused on the representation and optimization of the prestressing tendon within a concrete domain. [8] presented a two-dimensional (2D) beam with a single cable modeled using linear segments. This work was later extended by the same authors through the introduction of a B-spline-based cable parametrization and allowing for the minimization of the prestressing force. [9]

The topic has also been investigated by [10], who implemented a Drucker-Prager cri-

terion together with an alternative tendon parametrization, with an emphasis on low-complexity and manufacturable designs. Furthermore, [11] also developed a framework for the simultaneous optimization of the prestressing cable and the concrete structure, with the objective of minimizing tensile stresses. Their formulation also accounted for frictional losses associated with post-tensioning, which have previously been neglected.

The thesis is structured as follows. Section 2, 3 and 4 present the theoretical background on the finite element method and structural optimization. Section 5 describes the implementation and modeling of the existing optimization framework. Section 6 presents the addition of the stress constraint and Section 7 displays and discusses the result from 3 numerical examples. Lastly, Section 8 ends the report with conclusions and future work.

2 Finite Element Method for Linearly Elastic Materials

The Finite Element Method (FEM) is a computational tool for solving engineering problems such as stress and deformation analysis in geometrically complex structures. FEM replaces the continuous problem domain with a finite number of elements connected at discrete points called nodes. Within each element, the unknown field variables (such as displacements) are approximated using interpolation functions, also called shape functions. This approach allows for complex geometries, varying material properties, and boundary conditions to be handled efficiently.

For structural mechanics problems, the starting point is the balance of linear momentum. For a static problem with external body forces, the governing equation in strong form is:

$$\nabla \cdot \boldsymbol{\sigma} + \boldsymbol{b} = \mathbf{0} \tag{1}$$

Here, $\boldsymbol{\sigma}$ is the stress tensor and $\boldsymbol{b}$ is the body force vector per unit volume.

Directly solving the strong formulation requires the governing equations to be satisfied at every point in the domain, which is often impractical for complex problems. The weak formulation instead applies integration by parts, reducing the required order of derivatives in the solution. This makes it more flexible and suitable for numerical methods such as the FEM because it works well with solutions that are approximated piecewise over small elements rather than being represented by a single exact function over the entire domain. The weak form remains mathematically equivalent to the strong form while providing a formulation that is better suited for computational implementation.

The weak formulation is obtained by multiplying the strong form by an arbitrary weighting function $\boldsymbol{w}$ and integrating over the problem domain V:

$$\int_V \boldsymbol{w}^T \left(\nabla \cdot \boldsymbol{\sigma} + \boldsymbol{b}\right) \mathrm{d}V = 0 \tag{2}$$

Applying Gauss' divergence theorem to the stress term gives:

$$\int_V (\nabla \boldsymbol{w})^T \boldsymbol{\sigma} \, \mathrm{d}V - \int_S \boldsymbol{w}^T \boldsymbol{t} \, \mathrm{d}S + \int_V \boldsymbol{w}^T \boldsymbol{b} \, \mathrm{d}V = 0 \tag{3}$$

where S is the part of the boundary to V with traction $\boldsymbol{t}$.

The constitutive relation for a linearly elastic material is:

$$\boldsymbol{\sigma} = \boldsymbol{D}\boldsymbol{\epsilon} \tag{4}$$

The kinematic relation between strains and displacements is:

$$\boldsymbol{\epsilon} = \boldsymbol{B}\boldsymbol{u} \tag{5}$$

Here, $\boldsymbol{D}$ is the material stiffness matrix, $\boldsymbol{B}$ is the strain-displacement matrix and $\boldsymbol{u}$ is the displacement vector.

In the Galerkin method, the weighting functions are chosen to be the same as the shape functions used to approximate displacements:

$$\boldsymbol{u} \approx \boldsymbol{N}\boldsymbol{a} \tag{6}$$

where $\boldsymbol{N}$ is the shape function matrix and $\boldsymbol{a}$ contains the nodal displacement values.

Substituting the constitutive and kinematic relations, along with the displacement approximation, into the weak form and rearranging gives the discrete finite element system:

$$\boldsymbol{K}\boldsymbol{a} = \boldsymbol{f} \tag{7}$$

The global stiffness matrix $\boldsymbol{K}$ and load vector $\boldsymbol{f}$ are assembled from element contributions.

$$\boldsymbol{K}_e = \int_{V_e} \boldsymbol{B}^T \boldsymbol{D} \boldsymbol{B} \, \mathrm{d}V \tag{8}$$

$$\boldsymbol{f}_e = \int_{V_e} \boldsymbol{N}^T \boldsymbol{b} \, \mathrm{d}V + \int_S \boldsymbol{N}^T \boldsymbol{t} \, \mathrm{d}S \tag{9}$$

Once $\boldsymbol{a}$ is computed, strains and stresses in the structure can be determined from the kinematic and constitutive relations. [12]

3 Topology Optimization

Topology optimization is a computational design methodology aimed at determining the optimal material distribution within a prescribed design domain, subject to external loads, boundary conditions and problem-specific constraints. Using the same finite mesh as in the FEM, each element is prescribed a design variable. For a pseudo-density approach, this design variable represents if the element is solid (1) or void (0) of material.

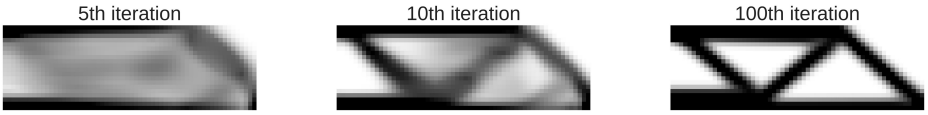

Figure 2: Simple topology optimization program. (Generated by code provided in [13].)

Like other optimization problems, the optimizer tries to minimize an objective function value while respecting a set of constraints. Topology optimization requires a fine mesh in order to capture detail and represent complex structures. This results in a mesh with a large number of design variables which renders heuristic or brute-force approaches computationally impractical. Consequently, gradient-based optimization methods are employed, as they exploit sensitivity information to iteratively improve and update the design variables. The optimization process thereby proceeds toward a local minimum of the objective function, subject to the imposed constraints, with each iteration requiring both a structural analysis to evaluate the current design and a sensitivity analysis to compute the gradients with respect to the design variables.

3.1 Optimization Loop

There exist many variations of the topology optimization loop, but most follow the same general structure shown below:

- Initialize design with densities $\boldsymbol{\rho}_{(1)}$
- For each iteration i until convergence:
  - Apply filtering and penalization to obtain $\bar{\boldsymbol{\rho}}_{(i)}$
  - Assemble global stiffness matrix $\boldsymbol{K}(\bar{\boldsymbol{\rho}}_{(i)})$ and load vector $\boldsymbol{f}$
  - Solve the equilibrium equation $\boldsymbol{K}\boldsymbol{u}_{(i)} = \boldsymbol{f}$
  - Compute strains $\boldsymbol{\epsilon}_{(i)}$ and stresses $\boldsymbol{\sigma}_{(i)}$
  - Evaluate objective $\phi_{(i)}$ and constraint $g_{(i)}$
  - Compute sensitivities $\partial\phi/\partial\boldsymbol{\rho}_{(i)}$ and $\partial g/\partial\boldsymbol{\rho}_{(i)}$
  - Update design variables with the optimizer to obtain $\boldsymbol{\rho}_{(i+1)}$
  - Check convergence based on change in densities $\|\boldsymbol{\rho}_{(i+1)} - \boldsymbol{\rho}_{(i)}\|$
- When convergence is reached, output the final design $\boldsymbol{\rho}$

3.2 Gradient-based optimizers

Gradient-based methods solve optimization problems by iteratively updating the design variables using first-order sensitivity information of the objective and constraint functions. However, using this information directly in a gradient descent scheme is

impractical due to the requirement of careful tuning of the step size and the lack of enforcing the constraints.

Instead, more advanced gradient-based optimizers reformulate the original problem into a sequence of explicit subproblems that locally approximates the objective and constraint functions. These subproblems improve numerical stability by restricting the range of where the first-order information is used and allowing the constraints to be accounted for.

One example of such advanced method is the Method of Moving Asymptotes (MMA) introduced in [14]. MMA constructs separable convex approximations of the objective and constraint functions using the first-order sensitivity together with an iteratively adapting set of asymptotes which allows for an efficient and numerically stable convergence, suitable for large problems with many variables such as topology optimization.

3.3 Sensitivity Analysis

The difficulty in computing sensitivities in topology optimization arises from the fact that the objective function typically depends on the design variables both explicitly and implicitly through the state variables. This dependency is usually in the form of

$$\phi = \phi\big(\boldsymbol{\rho}, \boldsymbol{u}(\boldsymbol{\rho})\big) \tag{10}$$

where $\boldsymbol{\rho}$ denotes the vector of design variables and $\boldsymbol{u}$ is the displacement vector.

Direct differentiation of ϕ with respect to $\boldsymbol{\rho}$ yields

$$\frac{\partial \phi}{\partial \boldsymbol{\rho}} = \frac{\partial \phi}{\partial \boldsymbol{\rho}} + \frac{\partial \phi}{\partial \boldsymbol{u}} \frac{\partial \boldsymbol{u}}{\partial \boldsymbol{\rho}} \tag{11}$$

where the term $\partial \boldsymbol{u}/\partial \boldsymbol{\rho}$ is computationally expensive to evaluate.

To avoid the explicit computation of this term, the adjoint method is employed. The method introduces an adjoint vector $\boldsymbol{\lambda}$ and makes use of the equilibrium residual

$$\boldsymbol{R}(\boldsymbol{\rho}) = \boldsymbol{K}(\boldsymbol{\rho})\, \boldsymbol{u}(\boldsymbol{\rho}) - \boldsymbol{f} = \boldsymbol{0} \tag{12}$$

which is satisfied for any admissible design.

The objective function is augmented by the residual in the form of a Lagrangian:

$$\bar{\phi} = \phi(\boldsymbol{\rho}, \boldsymbol{u}) + \boldsymbol{\lambda}^T \boldsymbol{R} \tag{13}$$

Differentiating $\bar{\phi}$ with respect to $\boldsymbol{\rho}$ gives

$$\frac{\partial \bar{\phi}}{\partial \boldsymbol{\rho}} = \frac{\partial \phi}{\partial \boldsymbol{\rho}} + \frac{\partial \phi}{\partial \boldsymbol{u}} \frac{\partial \boldsymbol{u}}{\partial \boldsymbol{\rho}} + \boldsymbol{\lambda}^T \left(\frac{\partial \boldsymbol{K}}{\partial \boldsymbol{\rho}} \boldsymbol{u} + \boldsymbol{K} \frac{\partial \boldsymbol{u}}{\partial \boldsymbol{\rho}} \right) \tag{14}$$

Rearranging the terms associated with $\partial \boldsymbol{u}/\partial \boldsymbol{\rho}$ yields

$$\frac{\partial \bar{\phi}}{\partial \boldsymbol{\rho}} = \frac{\partial \phi}{\partial \boldsymbol{\rho}} + \boldsymbol{\lambda}^T \frac{\partial \boldsymbol{K}}{\partial \boldsymbol{\rho}} \boldsymbol{u} + \left(\frac{\partial \phi}{\partial \boldsymbol{u}} + \boldsymbol{\lambda}^T \boldsymbol{K} \right) \frac{\partial \boldsymbol{u}}{\partial \boldsymbol{\rho}} \tag{15}$$

By selecting the adjoint vector $\boldsymbol{\lambda}$ such that

$$\boldsymbol{K}^T\boldsymbol{\lambda} = -\frac{\partial \phi}{\partial \boldsymbol{u}}^T \tag{16}$$

the term in parentheses vanishes, and the sensitivity expression reduces to

$$\frac{\partial \phi}{\partial \boldsymbol{\rho}} = \frac{\partial \phi}{\partial \boldsymbol{\rho}} + \boldsymbol{\lambda}^T \frac{\partial \boldsymbol{K}}{\partial \boldsymbol{\rho}} \boldsymbol{u} \tag{17}$$

3.4 Penalization

In practice, the design variable is not restricted to the discrete values 0 and 1, but is instead relaxed to take continuous values in the interval between 0 and 1 thereby enabling the use of gradient-based optimization algorithms. However, this relaxation introduces a discrepancy with physical reality since the optimizer may converge to solutions where some elements have intermediate values between 0 and 1 which represents the element not being void, but not completely solid either. Elements with intermediate densities are often referred to as gray regions. Since such regions do not correspond to physically realizable material states, the final design is required to exhibit a clear black-and-white distribution of material and void in order to satisfy the realism constraint.

One approach to addressing this issue is the Solid Isotropic Material with Penalization (SIMP) scheme, which reduces the effective stiffness of elements with intermediate densities. By penalizing the stiffness contribution of such gray elements, SIMP diminishes their structural efficiency and thereby discourages their presence in the final design. This removes the relative difference between intermediate and void elements, effectively guiding the optimizer toward black-and-white solutions and facilitating a clearer decision process.

3.5 Regularization

Regularization techniques play a critical role in obtaining physically meaningful and manufacturable designs. Without regularization, the optimization algorithm is prone to producing numerical artifacts such as checkerboard patterns and mesh-dependent solutions. Regularization aims to address these issues by controlling the spatial distribution of the design variables and promoting well-defined material-void boundaries. Two widely used approaches are density filtering and sharpness projection filtering.

3.5.1 Density Filtering

Density filtering is a spatial smoothing technique that modifies the raw design field by averaging each element's density with those of its neighbors within a prescribed radius. This process introduces a length scale into the optimization problem, meaning that the resulting design cannot contain features smaller than the chosen filter radius. As a consequence, the design becomes less sensitive to mesh resolution and numerical instabilities are suppressed.

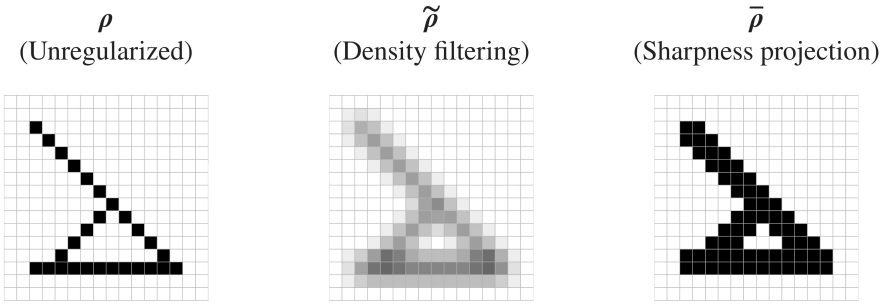

Figure 3: Simple demonstration of the most common regularization steps including a density filter and a sharpness projection filter.

The filter radius is a key parameter in this method. A larger radius enforces a coarser structural resolution, leading to smoother and thicker members, while a smaller radius allows for finer geometric features. The density filter also mitigates the occurrence of checkerboard patterns, which are artificial oscillations in the material distribution caused by the discretized finite element formulation.

3.5.2 Sharpness Projection Filter

While density filtering improves numerical stability and imposes a minimum feature size, it also tends to blur the transition between solid and void regions. This results in gray regions with intermediate values along the borders between material and voids. To counteract this effect, a projection filter based on a smooth approximation of the Heaviside step function is commonly applied after density filtering.

The purpose of the projection filter is to push filtered densities toward either 0 (void) or 1 (solid), thereby enhancing the sharpness of the structural boundaries. The projection is controlled by two main parameters: a threshold value, which determines the point around which the transition occurs, and a sharpness parameter, which controls how steep the transition is. A small sharpness parameter results in a gradual transition, while a large one produces a sharper, almost binary distribution.

In practical implementations, the sharpness parameter is often increased gradually during the optimization process. This continuation approach allows the optimizer to explore the design space freely in the early stages, while enforcing a nearly discrete material distribution in the final iterations. By combining density filtering with Heaviside projection, it is possible to achieve designs that are both numerically stable and practically realizable, with well-defined structural boundaries and a controlled feature size.

4 Shape Optimization

Shape optimization is another class of structural optimization, where the shape of the geometry is optimized instead of the material distribution as in topology optimization. The key difference is that shape optimization doesn't effect the connectivity of the structure. This means that the layout of the structure is already defined but the position or the shape of its parts are to be determined. The design variables therefore typically parameterize boundary node positions or geometric control points and no new holes or load paths can be introduced during the optimization process.

The methodology works essentially the same as for topology optimization. From the first-order derivatives of the objective function, the design variables are updated iteratively until a convergence is reached. The only practical difference is what the design variables actually stand for. Penalization and regularization of the shape design variables can also be applied according to the specific needs of the problem to achieve realistic and useful designs.

5 Current Optimization Framework

5.1 Modeling

The design domain comprises a structured mesh of regular hexahedral elements which is used both for the finite element analysis and the density distribution in the topology optimization for modeling of the concrete material. Each cell in the mesh is assigned a design variable ρ for the topology optimization.

Also, the shape of the tendon which prestresses the structure is modeled using several control points that are free to move in space. These points are then connected into a continuous line to form the tendon layout. In this case, a second order B-spline is used to create a smooth and differentiable line which is needed to express the prestressing effect.

The coordinates of these control points act as the design variable $\boldsymbol{X}_{cp} = \begin{bmatrix} x & y & z \end{bmatrix}$ for the shape optimization.

The force experienced by the elements are separated into four parts which accounts for the external loads, gravity and forces from the prestressed tendon. For more details on how these forces are derived and expressed, see [7].

- $\Rightarrow$ Force from prestressing $\boldsymbol{f}_p$
  Elements in which the tendon passes through experience a force from the curvature $f_{curvature}$. The curvature creates a distributed transverse force proportional to the eccentricity directed toward the center of the curvature. If the element is located at the design domain boundary, it also experiences an anchoring force f_{Anchor} which is applied tangentially to the tendon direction. Both the $f_{Curvature}$ and f_{anchor} are proportional to the tension force within the tendon T_{pre}. Figure 5 shows two elements which demonstrates these forces.

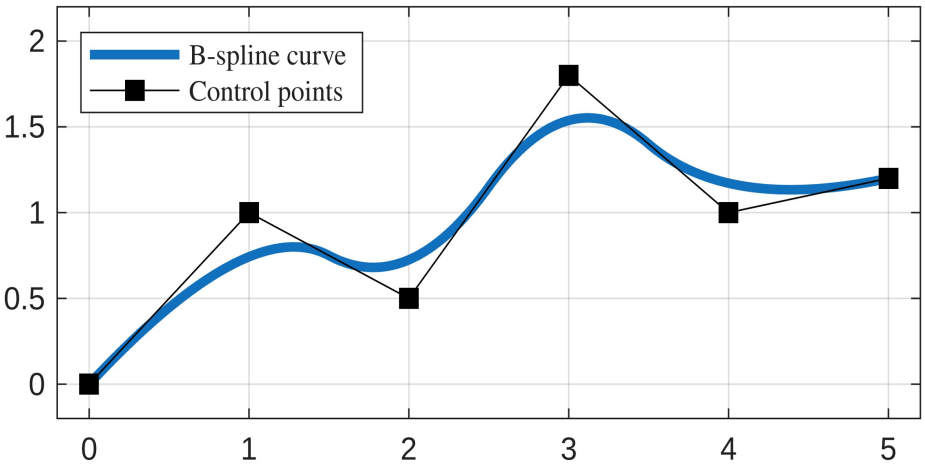

Figure 4: An arbitrary second-order B-spline visualization.

⇒ Force from self-weight $\boldsymbol{f}_s$
All elements experience some effect from gravity depending on the pseudo-density in the element. The self weight force f_s is calculated using the element pseudo-density, element volume and specific weight of the material.

⇒ External load forces $\boldsymbol{f}_d$ & $\boldsymbol{f}_l$
The dead load f_d together with the force from prestressing and self-weight compose the permanent load of the structure whereas the live load f_l is applied separately. Both $\boldsymbol{f}_d$ and $\boldsymbol{f}_l$ are identical and applies external loads unto the structure.

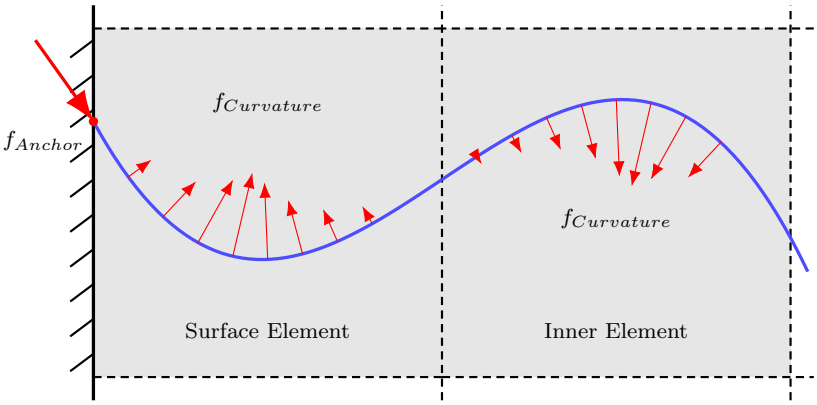

Figure 5: Two neighboring elements. Blue line indicates tendon shape inside two filled concrete elements, highlighting forces arising from the anchor and the curvature. Note that anchoring forces only act on boundary elements.

For simplicity hereafter, indexes p, s, $d \,\&\, l$ used in conjunction with forces $\boldsymbol{f}$ and displacements $\boldsymbol{u}$ represents the combination of said indexes. For example, $\boldsymbol{f}_{sdp}$ is

implying $\boldsymbol{f}_s + \boldsymbol{f}_d + \boldsymbol{f}_p$ and $\boldsymbol{u}_{sdp}$ contains the combined displacements from the self-weight, dead load and prestressing forces.

5.2 Filtering

The density design variables are filtered three times to remove artificial artifacts and provide realistic results. The filters also act as a physical coupling between the design variables used in the shape and topology optimization.

5.2.1 Density Filter

To mitigate the issues from mesh dependencies, a regularization filter is applied. Previously, this could be done using a smooth weighted density average function in conjunction with padding extra layers of surface elements around the design domain [15] [16].

The PDE filter is an improvement of the density filtering since it doesn't need to track neighboring elements which scales badly for a average weighting algorithm, especially in 3 dimensions. It does this by solving a Helmholtz type PDE with a Neumann boundary conditions which diffuses and smooths sharp variations in density. Another added benefit by this is to allow parallelization for applying the filter. The PDE filter still have issues with artificially sticking to the boundary surface [17].

A augmentation of the PDE filter was introduced by [18] where a Robin boundary condition was used instead to remove the boundary region issue. This resulted in smooth and computationally efficient filter with the removal of the previously needed padding layers. A parameter, r_s, was added to control the cost of applying material at the surfaces, making for simple and intuitive way to allow and disallow certain surface designs.

$$-r^2\nabla^2\tilde{\rho} + \tilde{\rho} = \rho \qquad\qquad r^2\nabla\tilde{\rho}\cdot\boldsymbol{n} = -r_s\tilde{\rho} \tag{18}$$

Here, r is a length scale parameter to control and $\boldsymbol{n}$ is the outward normal direction vector of the boundary element.

For elements on symmetry planes, r_s were set to zero while being set to $r_s = r$ on all other surfaces.

5.2.2 Cable-to-Concrete Filter

A cable-to-concrete filter is applied to ensure that tendons are fully embedded within the concrete domain. This is essential for physical realism, as the tension in the cable has minimal effect on the structure if it is not completely enclosed in concrete. The filter enforces this by driving the material density toward 1 within a specified filter radius around the tendon. As a result, concrete coverage is guaranteed in regions where tendons are placed, even if those regions are otherwise not optimal with respect to the objective functions or constraints.

The following Super-Gaussian function is used, the parameter μ can be tuned to create a sharper or smoother transition around the filter radius.

$$\hat{\rho} = \tilde{\rho} + (1 - \tilde{\rho}) \exp\left(-\frac{1}{2}\left(\frac{d^{min}}{r_{cf}}\right)^{\mu}\right) \tag{19}$$

r_{cf} is the cable-to-concrete filter radius and d_{min} is the shortest distance between the cable and the centroid of an element.

5.2.3 Heaviside Sharpness Projection Filter

The densities are filtered using the Heaviside sharpness projection method introduced to obtain eroded, intermediate and dilated designs. The eroded design represents a conservative version of the structure where material is removed at the boundaries while the dilated design is the expanded version with more material around the boundaries. The projection is defined as:

$$\bar{\rho}_i = \frac{\tanh(\beta_{HS}\eta_{HS}) + \tanh(\beta_{HS}(\hat{\rho}_i - \eta_{HS}))}{\tanh(\beta_{HS}\eta_{HS}) + \tanh(\beta_{HS}(1 - \eta_{HS}))} \tag{20}$$

where η_{HS} is the threshold parameter, and β_{HS} controls the sharpness of the projection. For the eroded and dilated layouts, threshold values $\eta_{HS}^{\text{ero}} = 0.6$ and $\eta_{HS}^{dil} = 0.4$ are used, respectively. An intermediate layout is obtained using $\eta_{HS}^{int} = 0.5$, which serves as the final design representation [19] [20].

In the robust formulation, finite element analysis and the stress constraint are applied to the eroded layout, while the volume constraint is enforced on the dilated one. This is to add a safety margin to ensure the final design is acceptable even under worst-case conditions. It should be noted that the eroded layout necessarily isn't the worst layout in every circumstance.

5.3 Finite Element Analysis

The structure is assumed to behave according to linear isotropic elasticity. To separate the material stiffness from the constitutive form, the constitutive matrix is decomposed as $\boldsymbol{D} = E\boldsymbol{D}_0$ where $\boldsymbol{D}_0$ is a normalized constitutive matrix depending only on Poisson's ratio ν. Accordingly, the Lamé parameters are written in normalized form as

$$\mu_0 = \frac{1}{2(1+\nu)}, \quad \lambda_0 = \frac{\nu}{(1+\nu)(1-2\nu)} \tag{21}$$

The resulting $\boldsymbol{D}_0$ in Voigt notation is:

$$\boldsymbol{D}_0 = \begin{bmatrix} 2\mu_0 + \lambda_0 & \lambda_0 & \lambda_0 & 0 & 0 & 0 \\ \lambda_0 & 2\mu_0 + \lambda_0 & \lambda_0 & 0 & 0 & 0 \\ \lambda_0 & \lambda_0 & 2\mu_0 + \lambda_0 & 0 & 0 & 0 \\ 0 & 0 & 0 & \mu_0 & 0 & 0 \\ 0 & 0 & 0 & 0 & \mu_0 & 0 \\ 0 & 0 & 0 & 0 & 0 & \mu_0 \end{bmatrix} \tag{22}$$

Penalisation of intermediate element densities is handled via the Solid Isotropic Material with Penalization (SIMP) method [21], where the effective Youngs modulus of each element is dependent on the eroded layout and a penalty factor p_E. Since the penalization is dependent on the design variable, each element needs a unique formulation of Young's modulus E_e.

$$E_e = E_{\min} + (E_0 - E_{\min})\,(\bar{\rho}_e^{\text{ero}})^{p_E} \tag{23}$$

The element stiffness matrix $\boldsymbol{K}^e$ is defined in Eq. 8 and is numerically integrated using Gauss quadrature into:

$$\boldsymbol{K}^e_{\text{ero}} = \sum_{i=1}^{N_{\text{gp}}} \boldsymbol{B}_i^{eT}\, E_e \boldsymbol{D}_0\, \boldsymbol{B}_i^e\, \det(J_i)\, w_i \tag{24}$$

where $N_{\text{gp}} = 8$ is the number of Gauss points, J_i is the Jacobian at Gauss point i, and w_i is the corresponding integration weight.

Once the element stiffness matrix $\boldsymbol{K}^e_{\text{ero}}$ has been computed through numerical integration, it is assembled into the global stiffness matrix $\boldsymbol{K}_{\text{ero}}$. The global system of equations takes the form:

$$\boldsymbol{K}_{\text{ero}} \boldsymbol{u}_{sdpl} = \boldsymbol{f}_s + \boldsymbol{f}_d + \boldsymbol{f}_p + \boldsymbol{f}_l \tag{25}$$

where $\boldsymbol{u}_{sdpl}$ is the global displacement vector and forces f with a index which represents the origin. The system is solved at each design iteration to obtain the displacement field which is subsequently used to evaluate the objective function and stress constraint.

5.4 Optimization Problem

The objective function ϕ is split into two parts. The first part ϕ_1 minimizes the displacement of nodes on the top of the structure under static conditions (indexes *sdp*). This is to prevent extreme bending in the opposite direction before applied load. The second part ϕ_1 is compliance minimization under the live load. The objective can thus be interpreted as a trade off between displacements from the live load with the displacement from the prestressing. Here, $\bar{\boldsymbol{l}}$ denotes a binary vector with nodes that are positioned on the top layer of the design domain.

$$\phi_1 = (\bar{\boldsymbol{l}} \cdot \boldsymbol{u}_{sdp})^T (\bar{\boldsymbol{l}} \cdot \boldsymbol{u}_{sdp}) \tag{26}$$

$$\phi_2 = \boldsymbol{f}_l \boldsymbol{u}_l \tag{27}$$

The original optimization problem can thus be formulated as followes.

$$\begin{cases} \min\limits_{\boldsymbol{\rho},\boldsymbol{X}} & \phi = \dfrac{w_1}{\phi_1^0}\phi_1 + \dfrac{w_2}{\phi_2^0}\phi_2 \\ \text{s.t.} & g_1 = V(\bar{\rho}_{dil}) - V^*_{dil} \le 0 \\ & 0 \le \rho_e \le 1, \quad e = 1, 2, \ldots, N_e \\ & \underline{\boldsymbol{X}} \le \boldsymbol{X} \le \overline{\boldsymbol{X}} \\ \text{with} & \boldsymbol{K}_{\text{ero}} \boldsymbol{u}_{sdpl} = \boldsymbol{f}_s + \boldsymbol{f}_d + \boldsymbol{f}_p + \boldsymbol{f}_l \end{cases} \tag{28}$$

where $V^*_{dil} = [V(\bar{\rho}_{dil}) \cdot V^*_{int}] / V(\bar{\rho}_{int})$ represents the maximum allowable volume fraction based on the dilated layout which is different from the maximum allowable volume fraction based on the intermediate layout V^*_{int} set by the user. w/ϕ_0 are the weight and scaling coefficients to produce an objective value of 1 on the initial design. The density is kept between 0 and 1 while the shape optimization variables are restricted by the lower and upper bound, $\underline{\boldsymbol{X}}$ and $\overline{\boldsymbol{X}}$ respectively.

The optimizer used is based on the Method of Moving Asymptotes (MMA) [14]. The optimization ends when the criteria for convergence is met. The criteria is based on the absolute changes in objective and constraint values being lower than 10^{-4} for three consecutive iterations. The maximum number of iterations is set to 100 if the criteria isn't fulfilled.

5.5 Objective and volume constraint sensitivities

The objective function and the volume constraint are kept the same as in the original paper, thus keeping the same derivatives. The objective function is expanded with the adjoint vector and residual from the static equilibrium to form the augmented objective function.

$$\hat{\phi} = \frac{w_1}{\phi_1^0}(\boldsymbol{l} \cdot \boldsymbol{u}_{sdp})^T(\boldsymbol{l} \cdot \boldsymbol{u}_{sdp}) + \frac{w_2}{\phi_2^0}\boldsymbol{f}_l \boldsymbol{u}_l \tag{29}$$

$$+ \boldsymbol{\lambda}_1^T(\boldsymbol{K}_{\text{ero}}\boldsymbol{u}_{sdp} - \boldsymbol{f}_s - \boldsymbol{f}_d - \boldsymbol{f}_p) + \boldsymbol{\lambda}_2^T(\boldsymbol{K}_{\text{ero}}\boldsymbol{u}_l - \boldsymbol{f}_l) \tag{30}$$

This function is differentiated with respect to both design variables which results in the following adjoint equations to eliminate the problematic terms.

$$\boldsymbol{K}_{\text{ero}}\boldsymbol{\lambda}_1 = -2\frac{w_1}{\phi_1^0}(\boldsymbol{l} \cdot \boldsymbol{u}_{sdp} \cdot \boldsymbol{l}) \tag{31}$$

$$\boldsymbol{K}_{\text{ero}}\boldsymbol{\lambda}_2 = -\frac{w_2}{\phi_2^0}\boldsymbol{f}_l \tag{32}$$

Substitution of the adjoint vectors into the differentiated objective function yields the following derivative with respect to the eroded density. The terms $\boldsymbol{f}_d$ and $\boldsymbol{f}_l$ are independent of the filtered density, while $\boldsymbol{f}_s$ and $\boldsymbol{K}_{\text{ero}}$ depend on the eroded density. The prestressing force $\boldsymbol{f}_p$ depends solely on the shape design.

This leads to further simplification and allows us to represent:

$$\hat{\phi} = \hat{\phi}(\bar{\boldsymbol{\rho}}_{\text{ero}}, \boldsymbol{X}) \tag{33}$$

Hence, the total derivatives are computed via the chain rule as:

$$\frac{d\hat{\phi}}{d\boldsymbol{\rho}} = \frac{\partial\hat{\phi}}{\partial\bar{\boldsymbol{\rho}}_{\text{ero}}}\frac{\partial\bar{\boldsymbol{\rho}}_{\text{ero}}}{\partial\boldsymbol{\rho}} \tag{34}$$

$$\frac{d\hat{\phi}}{d\boldsymbol{X}} = \frac{\partial\hat{\phi}}{\partial\bar{\boldsymbol{\rho}}_{\text{ero}}}\frac{\partial\bar{\boldsymbol{\rho}}_{\text{ero}}}{\partial\boldsymbol{X}} + \frac{\partial\hat{\phi}}{\partial\boldsymbol{X}} \tag{35}$$

The partial derivative of $\hat{\phi}$ with respect to the eroded density is:

$$\frac{\partial \hat{\phi}}{\partial \boldsymbol{\rho}_{\text{ero}}} = \boldsymbol{\lambda}_1^T \left[\frac{\partial \boldsymbol{K}_{\text{ero}}}{\partial \boldsymbol{\rho}_{\text{ero}}} \boldsymbol{u}_{sdp} - \frac{\partial \boldsymbol{f}_s}{\partial \boldsymbol{\rho}_{\text{ero}}} \right] - \frac{w_1}{\phi_2^0} \boldsymbol{u}_l^T \frac{\partial \boldsymbol{K}_{\text{ero}}}{\partial \boldsymbol{\rho}_{\text{ero}}} \boldsymbol{u}_l \tag{36}$$

The partial derivative with respect to the shape design variables is:

$$\frac{\partial \hat{\phi}}{\partial \boldsymbol{X}} = -\boldsymbol{\lambda}_1 \frac{\partial \boldsymbol{f}_p}{\partial \boldsymbol{X}} \tag{37}$$

The volume constraint is a function of the diluted density and the derivatives then become:

$$\frac{dg_1}{d\boldsymbol{\rho}} = \frac{\partial g_1}{\partial \bar{\boldsymbol{\rho}}_{dil}} \frac{\partial \bar{\boldsymbol{\rho}}_{dil}}{\partial \boldsymbol{\rho}} \tag{38}$$

$$\frac{dg_1}{d\boldsymbol{X}} = \frac{\partial g_1}{\partial \bar{\boldsymbol{\rho}}_{dil}} \frac{\partial \bar{\boldsymbol{\rho}}_{dil}}{\partial \boldsymbol{X}} \tag{39}$$

6 Stress Constraint

The stress tensor is defined in Voigt notation as:

$$\boldsymbol{\sigma} = \begin{bmatrix} \sigma_{xx} & \sigma_{yy} & \sigma_{xx} & \sigma_{xy} & \sigma_{yz} & \sigma_{zx} \end{bmatrix}^T \tag{40}$$

The constitutive equation is used to calculate the stress knowing the strains [12]:

$$\boldsymbol{\sigma} = E_e \boldsymbol{D}_0 \boldsymbol{\epsilon} \tag{41}$$

The strain can be substituted with displacements $\boldsymbol{\epsilon} = \boldsymbol{B}_i^e \boldsymbol{u}_{sdpl}^e$ which results in the following equation:

$$\boldsymbol{\sigma}_i^e = E_e \boldsymbol{D}_0 \boldsymbol{B}_{\boldsymbol{i}}^{\boldsymbol{e}} \boldsymbol{u}_{\boldsymbol{sdpl}}^{\boldsymbol{e}} \tag{42}$$

6.1 Drucker-Prager yield criterion

The Drucker-Prager yield function [22] extends the von Mises yield criterion [23] by incorporating a dependence on pressure, modeled through the hydrostatic pressure I_1. Here, I_1 is the first stress invariant, J_2 is the second deviatoric stress invariant and $\boldsymbol{\sigma}$ is the stress vector.

$$F(\boldsymbol{\sigma}) = \sqrt{3J_2(\boldsymbol{\sigma})} + \alpha I_1(\boldsymbol{\sigma}) - \beta \leq 0 \tag{43}$$

$$I_1 = \sigma_{xx} + \sigma_{yy} + \sigma_{zz} \tag{44}$$

$$J_2 = 1/6 \left[(\sigma_{xx} - \sigma_{yy})^2 + (\sigma_{yy} - \sigma_{zz})^2 + (\sigma_{zz} - \sigma_{xx})^2 \right] + 2\sigma_{xy}^2 + 2\sigma_{yz}^2 + 2\sigma_{zx}^2 \tag{45}$$

The material parameters α and β are defined such that when the tensile yield strength is the same as the compressive yield strength, $\sigma_t = \sigma_c$, the von Mises yield function is

recovered with $\alpha = 0$ and $\beta = \sigma_t$. In this case, the pressure dependency is eliminated, as there no longer exists any directional favorability. It can be observed that β has the unit of stress and represents the yield limit, while α is dimensionless and characterizes the level of pressure sensitivity. α and β can be derived from Eq. 43 for the case when the material is yielding in uniaxial tension, σ_t, and for another case when in uniaxial compression, σ_c. For later comparison purposes, the variable s_{ct} is introduced to keep track of the compression-to-tension yield limit ratio $s_{ct} = \sigma_c/\sigma_t$.

Uniaxial tension: $\boldsymbol{\sigma} = \begin{bmatrix}\sigma_t & 0 & 0 & 0 & 0 & 0\end{bmatrix}^T$

$$\iff F(\boldsymbol{\sigma}) = \sqrt{\sigma_t^2} + \alpha\,\sigma_t - \beta = 0 \tag{46}$$

Uniaxial compression: $\boldsymbol{\sigma} = \begin{bmatrix}0 & -\sigma_c & 0 & 0 & 0 & 0\end{bmatrix}^T$

$$\iff F(\boldsymbol{\sigma}) = \sqrt{\sigma_c^2} - \alpha\,\sigma_c - \beta = 0 \tag{47}$$

Combining Eq. 46 and 47 gives the following equations for the constants.

$$\alpha = \frac{\sigma_c - \sigma_t}{\sigma_c + \sigma_t} \tag{48}$$

$$\beta = 2\frac{\sigma_c\sigma_t}{\sigma_c + \sigma_t} \tag{49}$$

The Drucker-Prager yield criteria can be visualized as a circular cone surface in the principle stress space $(\sigma_1, \sigma_2, \sigma_3)$ as shown in Figure 6. Here, it is clear that the Drucker-Prager yield surface is not only limited in tension, but also tolerates far higher compressive loads than the von Mises equivalent as part of the pressure direction dependency.

For convenience, the yield function is normalized with the yield limit β for improved clarity and scalability. The yield function thus becomes:

$$\bar{F}(\boldsymbol{\sigma}) = \frac{\sqrt{3J_2(\boldsymbol{\sigma})} + \alpha I_1(\boldsymbol{\sigma})}{\beta} - 1 \leq 0 \tag{50}$$

6.2 Relaxation

ϵ-relaxation is a method developed by [24] to alleviate the issue of stress singularities. The stress singularity issue arises when the displacement in a near-zero density element is non-negligible, causing stress values which violate the constraint. This is problematic since it can hinder element densities from approaching zero. A new variable h_e is introduced to handle the relaxation. For elements with a near-zero density, h_e will mark them as non-yielding despite potentially exhibiting artificial stress peaks caused by singularities.

$$h_e(\bar{\rho}_e^{\text{ero}}) = 1 + \frac{\epsilon}{\bar{\rho}_e^{\text{ero}}} - \epsilon \tag{51}$$

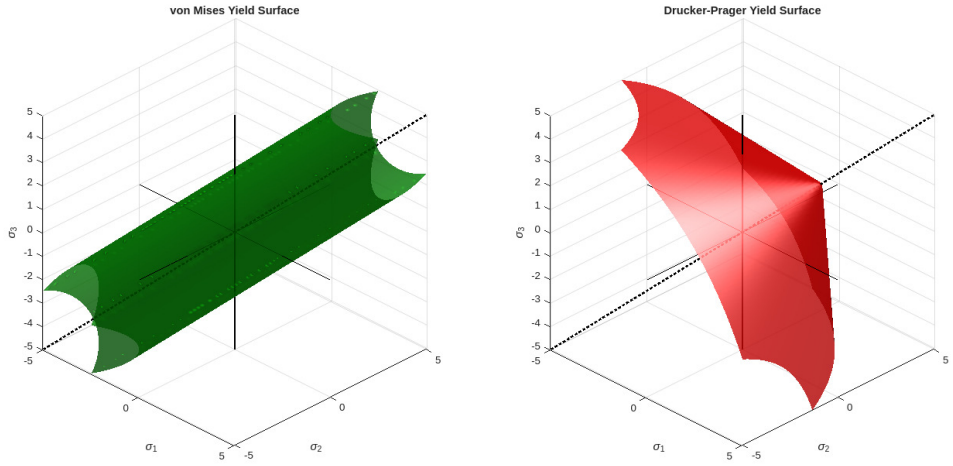

Figure 6: Comparison of yield surfaces in the principal stress space. Left: von Mises yield surface. Right: Drucker-Prager yield surface.

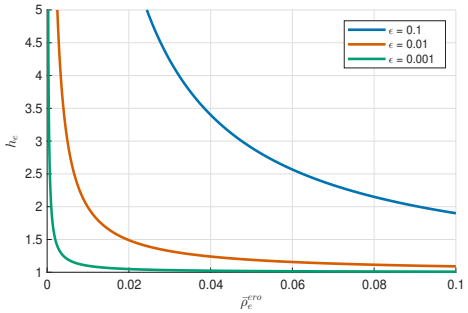

Figure 7: h_e as a function of $\bar{\rho}_e^{\text{ero}}$ for $\epsilon = \{0.1, 0.01, 0.001\}$.

This affects the yield function which takes a new form and a dependency on the eroded density. It is thus both dependent on stress at every integration point as well as the element density.

$$\bar{F}(\boldsymbol{\sigma}, \bar{\rho}_e^{\text{ero}}) = \frac{\sqrt{3J_2(\boldsymbol{\sigma})} + \alpha I_1(\boldsymbol{\sigma})}{\beta} - h_e(\bar{\rho}_e^{\text{ero}}) \leq 0 \tag{52}$$

ϵ is a positive non-zero value chosen such that is small enough to not intervene with the regular constraints, but also large enough to relax the low-density elements. ϵ in the context of relaxation should not be confused with the strain $\boldsymbol{\epsilon}$. Figure 7 shows the influence of ϵ in Eq. 51 as the density approaches zero. The value $\epsilon = 0.01$ was chosen and kept constant during the project.

6.3 Aggregation

With the final form of the yield criterion finalized in Eq. 52, the constraint can be implemented.

$$g_i = \bar{F}_i(\boldsymbol{\sigma}_i, \bar{\rho}_e^{\text{ero}}) \leq 0 \tag{53}$$

The stress constraint is local since a unique stress state is calculated at every integration point. However, the sheer number of constraints makes the local stress constraint problem computationally inefficient to solve. The ideal solution to this would be to pick out the maximum value as the constraint.

$$g = \max(\bar{F}_i) \leq 0 \tag{54}$$

The problem with this constraint is the discontinuous nature of the max function. This results in a non-differentiable constraint function which can not be used in the gradient-based optimization. To overcome this, an aggregation function can be used to approximate the maximum stress. This results in a constraint which is smooth and significantly more efficient to solve than constraining every integration point.

There exists many different aggregation functions such as the P-norm or Kresselmeier-Steinhauser (KS) function [25]. These functions have different characteristics which makes the function more or less suitable to use in specific cases. The P-norm is perhaps the simplest form of approximation but requires special handling of negative numbers since it only can approximate absolute numbers. Therefore, to simplify the process, KS was used instead.

$$G_{KS} = \frac{1}{\eta} \ln \left[\sum_i \exp(\eta \bar{F}_i) \right] \tag{55}$$

The KS function utilizes a penalty parameter η to improve accuracy of the approximation by making the difference between the values larger. However, large values of η or F_i can easily overflow the computers memory of $\exp(\eta \bar{F}_i)$ which is why logarithmic laws are used to modify it into a computationally friendlier version.

$$G_{KS} = \bar{F}_{max} + \frac{1}{\eta} \ln \sum_i \exp\left[\eta(\bar{F}_i - \bar{F}_{max})\right] \tag{56}$$

This version offers better numerical stability and shows clearly how the KS-function will always return a larger number than the actual maximum. The penalty parameter η were set to 50 for all examples later in the report.

6.4 Sensitivity Analysis

The stress constraint g_2 is implemented upon the KS aggregation of all local stress fields through the yield function.

$$g_2 = \bar{F}_{max} + \frac{1}{\eta} \ln \sum_i \exp\left[\eta(\bar{F}_i - \bar{F}_{max})\right] \leq 0 \tag{57}$$

Since there are more design variables than constraints, the adjoint method of finding the sensitivities is utilized. The constraint equation g_2 can be augmented, $\hat{g}_2$, with an adjoint vector $\boldsymbol{\lambda}$ together with a residual equation based on static equilibrium:

$$\hat{g}_2 = g_2(\bar{\boldsymbol{\rho}}^{\text{ero}}, \boldsymbol{u}) + \boldsymbol{\lambda}^T \boldsymbol{R} \tag{58}$$

$$\boldsymbol{R} = \boldsymbol{K}_{\text{ero}}\boldsymbol{u} - \boldsymbol{f}_s - \boldsymbol{f}_d - \boldsymbol{f}_p - \boldsymbol{f}_l = \boldsymbol{0} \tag{59}$$

Since the stress is computed from displacements, the constraint can be expressed entirely in terms of eroded densities and displacements. The displacements are functions of the eroded density $\boldsymbol{u}(\bar{\boldsymbol{\rho}}^{\text{ero}})$, which in turn depends on both topological and shape design variables: $\bar{\boldsymbol{\rho}}^{\text{ero}}(\boldsymbol{\rho}, \boldsymbol{X})$.

When differentiating, the external live and dead loads are considered independent, while the prestressing force depends only on the shape variables, and self-weight depends on the eroded density. With respect to the density, the chain rule yields the following:

$$\frac{\partial \hat{g}_2}{\partial \boldsymbol{\rho}} = \frac{\partial g_2}{\partial \boldsymbol{\rho}} + \frac{\partial g_2}{\partial \boldsymbol{u}}\frac{\partial \boldsymbol{u}}{\partial \boldsymbol{\rho}} + \boldsymbol{\lambda}^T \left[\boldsymbol{K}_{\text{ero}} \frac{\partial \boldsymbol{u}}{\partial \boldsymbol{\rho}} + \frac{\partial \boldsymbol{K}_{\text{ero}}}{\partial \boldsymbol{\rho}}\boldsymbol{u} - \frac{\partial \boldsymbol{f}_s}{\partial \boldsymbol{\rho}} \right] \tag{60}$$

And similarly for the shape design variables:

$$\frac{\partial \hat{g}_2}{\partial \boldsymbol{X}} = \frac{\partial g_2}{\partial \boldsymbol{X}} + \frac{\partial g_2}{\partial \boldsymbol{u}}\frac{\partial \boldsymbol{u}}{\partial \boldsymbol{X}} + \boldsymbol{\lambda}^T \left[\boldsymbol{K}_{\text{ero}} \frac{\partial \boldsymbol{u}}{\partial \boldsymbol{X}} + \frac{\partial \boldsymbol{K}_{\text{ero}}}{\partial \boldsymbol{X}}\boldsymbol{u} - \frac{\partial \boldsymbol{f}_s}{\partial \boldsymbol{X}} - \frac{\partial \boldsymbol{f}_p}{\partial \boldsymbol{X}} \right] \tag{61}$$

To eliminate the problematic terms $\frac{\partial \boldsymbol{u}}{\partial \boldsymbol{\rho}}$ and $\frac{\partial \boldsymbol{u}}{\partial \boldsymbol{X}}$, the adjoint equation is introduced:

$$\boldsymbol{K}_{\text{ero}}\boldsymbol{\lambda} = -\left(\frac{\partial g_2}{\partial \boldsymbol{u}}\right)^T \tag{62}$$

The differentiation can be expanded using the chain rule to the following expression.

$$\frac{\partial g_2}{\partial \boldsymbol{u}_j} = \frac{\partial g_2}{\partial \bar{F}}\frac{\partial \bar{F}}{\partial \boldsymbol{\sigma}}\frac{\partial \boldsymbol{\sigma}}{\partial \boldsymbol{u}} \tag{63}$$

Which can also be assembled element-wise into the form:

$$\left(\frac{\partial g_2}{\partial \boldsymbol{u}}\right)_e = \sum_{i=1}^{N_{\text{gp}}} \left[\frac{\exp\left(\eta \bar{F}_{e,i}\right)}{\sum_{k=1}^{N_{\text{el}}}\sum_{l=1}^{N_{\text{gp}}} \exp\left(\eta \bar{F}_{k,l}\right)} \frac{1}{\beta} \left(\frac{3}{2} \cdot \frac{\boldsymbol{\sigma}_{\text{dev},e,i}}{\sqrt{3J_{2,e,i}}} + \alpha \boldsymbol{I} \right) E_e \boldsymbol{D}_0 \boldsymbol{B}_{e,i} \right] \tag{64}$$

Here, σ_{dev} is the deviatoric stress vector, N_{gp} the number of integration points per element and N_{el} the total number of elements.

For the design variables, explicit differentiation is done similarly.

$$\frac{\partial g_2}{\partial \bar{\rho}_e^{\text{ero}}} = \sum_{i=1}^{N_{\text{gp}}} \frac{\exp\left(\eta \bar{F}_{e,i}\right)}{\sum_{k=1}^{N_{\text{el}}} \sum_{l=1}^{N_{\text{gp}}} \exp\left(\eta \bar{F}_{k,l}\right)} \left[\frac{1}{\beta} \left(\frac{3}{2} \cdot \frac{\boldsymbol{\sigma}_{\text{dev},e,i}}{\sqrt{3J_{2,e,i}}} + \alpha \boldsymbol{I} \right) \frac{\partial E_e}{\partial \bar{\rho}_e^{\text{ero}}} \boldsymbol{D}_0 \boldsymbol{B}_{e,i} \boldsymbol{u}_e - \frac{\epsilon}{\left(\bar{\rho}_e^{\text{ero}}\right)^2} \right] \tag{65}$$

Finally, insertion into the augmented sensitivities gives:

$$\frac{\partial \hat{g}_2}{\partial \boldsymbol{\rho}} = \frac{\partial g_2}{\partial \bar{\boldsymbol{\rho}}_{\text{ero}}} \frac{\partial \bar{\boldsymbol{\rho}}_{\text{ero}}}{\partial \boldsymbol{\rho}} + \boldsymbol{\lambda}^T \left[\frac{\partial \boldsymbol{K}_{\text{ero}}}{\partial \boldsymbol{\rho}} \boldsymbol{u} - \frac{\partial \boldsymbol{f}_s}{\partial \boldsymbol{\rho}} \right] \tag{66}$$

$$\frac{\partial \hat{g}_2}{\partial \boldsymbol{X}} = \frac{\partial g_2}{\partial \bar{\boldsymbol{\rho}}_{\text{ero}}} \frac{\partial \bar{\boldsymbol{\rho}}_{\text{ero}}}{\partial \boldsymbol{X}} + \boldsymbol{\lambda}^T \left[\frac{\partial \boldsymbol{K}_{\text{ero}}}{\partial \boldsymbol{X}} \boldsymbol{u} - \frac{\partial \boldsymbol{f}_s}{\partial \boldsymbol{X}} - \frac{\partial \boldsymbol{f}_p}{\partial \boldsymbol{X}} \right] \tag{67}$$

7 Numerical Examples and Discussion

The examples are based on a simply supported beam. The first example is a showcase of the stress constraint by comparing the result with the stress constraint active and inactive. The second example is comparing how the ratio between the compressive and tensile strength affect the final design. And lastly, the third example compares different prestressing forces.

The concrete was modeled using a specific weight of 25 kN/m^3, Young's modulus of $E_0 = 30$ GPa and a Poison's ratio of $\nu = 0.2$. For the SIMP, the penalty factor were $p_E = 3$ and the minimum Young's modulus $E_{\text{min}} = 1$ Pa. To improve convergence, the sharpness parameter β_{HS} of the Heaviside projection filter were increased starting from 1 to 2, 4 and 8 at the 20th, 40th and 60th optimization iteration. The sharpness parameter of the cable-to-concrete filter were set to $\mu = 1$.

The initial designs are produced after setting all densities to 0.5, control points to the depthwise midpoint and then passing it through all the filters. Move limits were used to prevent too large changes through each iteration with the density move limit being 0.2 and the control point move limit dependent on the domain geometry.

The load for the cases were set to $q = 2$ kN/m^2 and the tendon prestressing force was $T_{\text{pre}} = 2$ kN unless specified otherwise. This is significantly less than the values used in [7] which is due to the application of the anchoring prestressing force. As shown in 5, the anchoring force is applied to a single edge element which imposes significant pressure to said element leading to yielding. To overcome this, the prestressing force was lowered which in turn decreased the deflection and thus reduced the loading capacity before yielding.

The optimization problem could thus be stated on the following form including the stress constraint aggregation from Eq. 56.

$$
\begin{cases}
\min\limits_{\boldsymbol{\rho},\boldsymbol{X}} & \phi = \dfrac{w_1}{\phi_1^0}\phi_1 + \dfrac{w_2}{\phi_2^0}\phi_2 \\
\text{s.t.} & g_1 = V(\bar{\rho}_{dil}) - V_{dil}^* \leq 0 \\
& g_2 = G_{KS} \leq 0 \\
& 0 \leq \rho_e \leq 1, \quad e = 1, 2, \ldots, N_e \\
& \underline{\boldsymbol{X}} \leq \boldsymbol{X} \leq \overline{\boldsymbol{X}} \\
\text{with} & \boldsymbol{K}_{\text{ero}}\boldsymbol{u}_{sdpl} = \boldsymbol{f}_s + \boldsymbol{f}_d + \boldsymbol{f}_p + \boldsymbol{f}_l
\end{cases}
\tag{68}
$$

7.1 Inactive vs. Active Stress Constraint

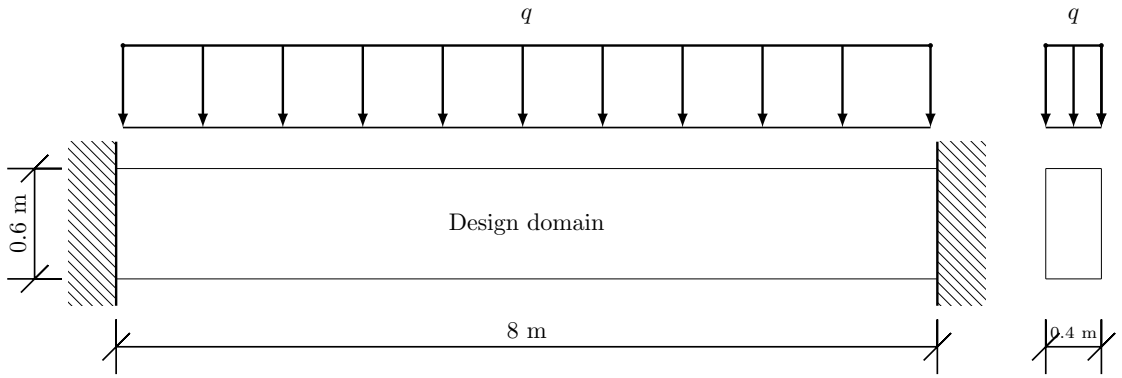

Figure 8: Design domain with supports and loading.

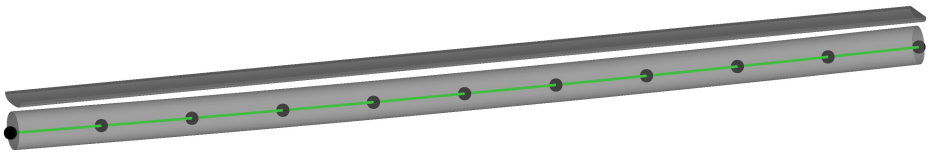

Figure 9: Initial design.

The design domain for the full beam had dimensions $8 \times 0.4 \times 0.6$ m with 11 evenly spaced control points for the design variables used for the shape optimization. Quarter symmetry was utilized by placing symmetry planes at the midpoints of the length and width. The quarter was modeled with 6 control points and a $160 \times 8 \times 24$ density mesh for the optimization consisting of a structured regular cubic elements with side length 0.025 m. Each element have 8 nodes, with $2 \times 2 \times 2$ integration points for improved numerical accuracy.

Two structures were produced with identical settings with exception to whether the stress constraint were active or not. The maximum allowable volume fraction in the intermediate layout were set to $V_{int}^* = 0.3$. The parameters for the stress measurements

were $\sigma_t = 5$ MPa for the tensile strength and $\sigma_c = 5 \times \sigma_t = 25$ MPa for the compressive strength. The PDE filter radius were $r = 0.1$ m as was the cable-to-concrete filter radius $r_{cf} = 0.1$ m. A box constraint prevents the control points from being closer than 0.05 m from the surfaces and a move limit of 0.1 m prevents rash movements.

The visual density distribution differences in Figures 10a and 10b are subtle but noticeable in the connections between the top and bottom part. A interesting difference is the placement of the control points where the stress constrained case resulted in a even curve across the whole length in contrast to the inactive case where the curvature is exclusive to outer part of the structure.

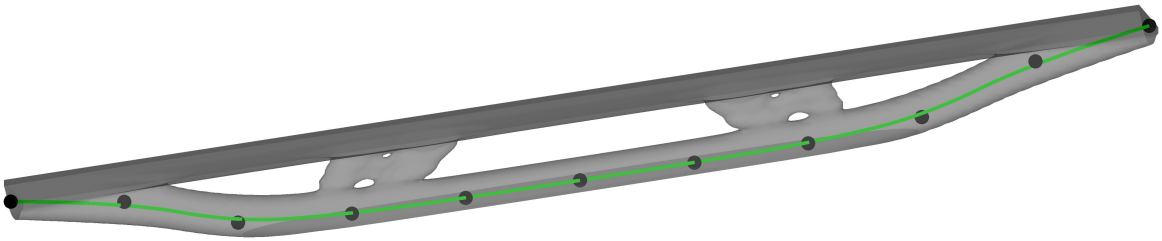

(a) Inactive stress constraint

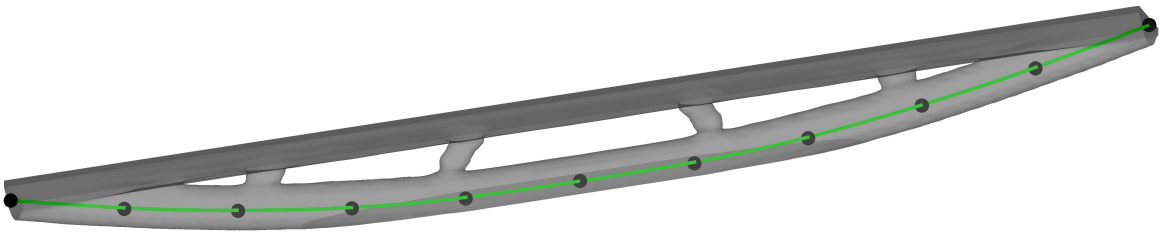

(b) Active stress constraint

Figure 10: Final beam designs.

The difference between the two runs becomes clearer in the function convergence history diagrams in Figure 11. Here, it is possible to see a difference in the constraint function g_2 which was simulated for the inactive case. The convergence also shows major disturbances at the 40th and 60th iteration in both cases when the Heaviside sharpness parameter was increased. This resulted in large spikes which eventually recovered a few iterations later. Both cases also didn't experience smooth convergences seen by the jagged lines. Neither case triggered the convergence condition and stopped at the maximum number of iterations.

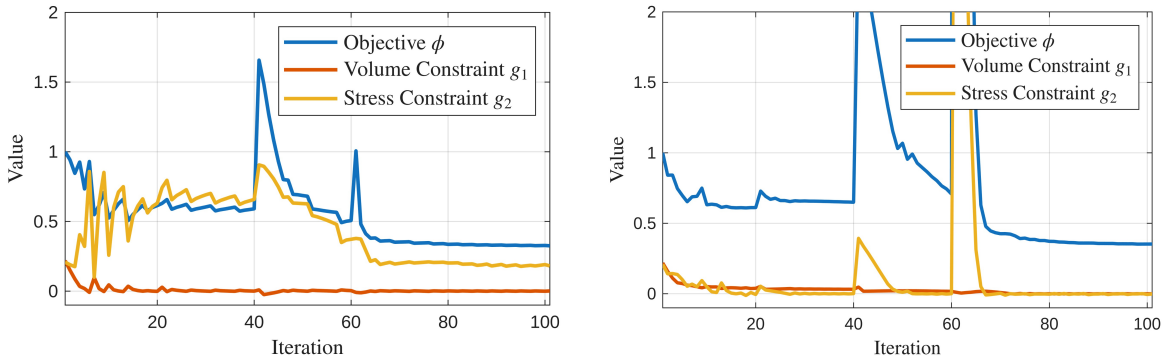

(a) Inactive stress constraint

(b) Active stress constraint

Figure 11: Function convergence histories. Heaviside sharpness factor ramps up at the 20th, 40th and 60th iteration.

Table 1 highlights the objective and constraint values during the two runs. The first case with inactive stress constraint clearly violates the yield limit with a normalized value of $g_2 = 0.1811$. The volume constraint is also violated with less than 1% which could be a sign that the optimizer hadn't fully converged on a solution within the maximum number of iterations. The table also shows that the active case performed worse in the objective functions. The vertical displacement due to permanent loads u_{sdp} and live load u_{l} were also higher in the node placed at the bottom of structure in the middle both length- and widthwise. All this indicates a lowered effect from the prestressing as well as a less stiff structure in the active case.

Design	$\tilde{\phi}$ [-]	ϕ_1 [m^2]	ϕ_2 [kNm]	g_1 [m^3]	g_2 [-]	u_{sdp} [mm]	u_{l} [mm]
Initial	1.0000	0.0635	0.0099	0.2188	0.2081	-	-
Inactive	0.3254	0.0078	0.0052	0.0015	0.1812	-3.1433	-1.8050
Active	0.3528	0.0092	0.0055	-0.0004	-0.0014	-3.4598	-2.0134

Table 1: Function value comparisons between the initial design with the two runs of inactive and active stress constraint. Displacements were from the bottom-most midpoint node.

A histogram over all finite elements with the yield limit mean value from the 8 integration points are shown in Figure 12 which quantifies how many elements that were violating the yield limit. In addition to the stress constraint function g_2, the actual maximum yield function value is shown to highlight the approximation error of the KS aggregation. Here, it can be seen a gap between the mean element yield value and the actually maximum yield value calculated at a single integration point. This shows that not all integration points within a element yields to the same degree. It should be said that even though this gap exists here, there were elements with mean averages of yield function values above the threshold anyways.

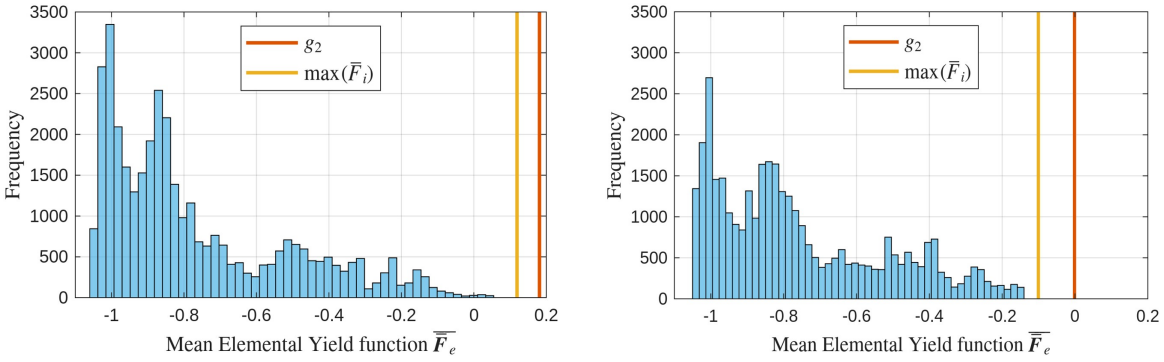

(a) Inactive stress constraint

(b) Active stress constraint

Figure 12: Histogram over yield functions for all elements. All integrations points are averaged to a mean yield function value.

7.2 Different values of s_{ct}

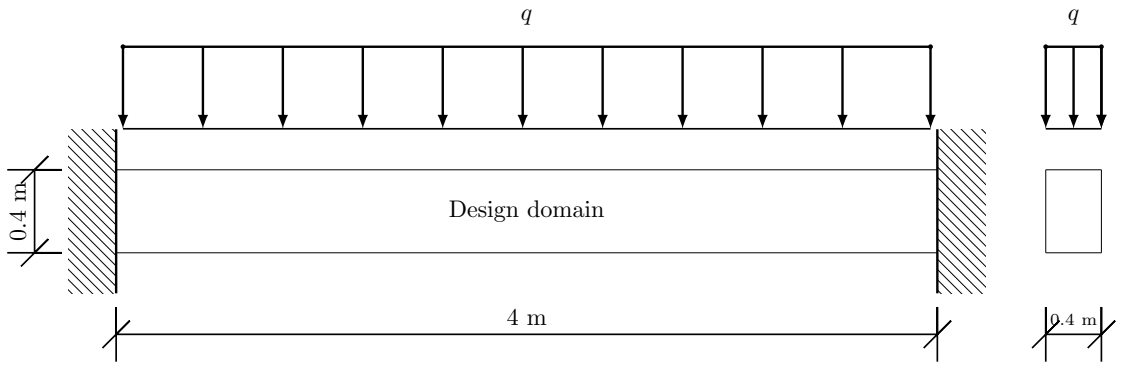

Figure 13: Design domain with supports and loading.

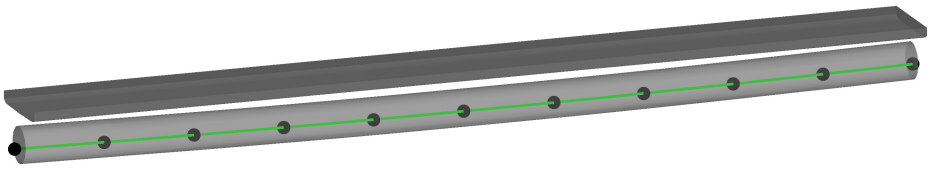

Figure 14: Initial design.

For the next example, two different ratios of $s_{ct} = \sigma_c/\sigma_t$ will be explored. The first case uses the fact that the Drucker-Prager yield function reduces to the von Mises yield criteria when $s_{ct} = 1$ while the second case use a more extreme ratio $s_{ct} = 10$. An average yield stress limit was introduced to make the comparison more fair. Using $(\sigma_t + \sigma_c)/2 = 15$ MPa resulted in the first case have a tensile strength of $\sigma_t = 15$ MPa and the second case $\sigma_t = 2.73$ MPa.

This example utilized a smaller design domain but still operating on the same principles as the previous example. The density mesh for the quarter was reduced to $80 \times 8 \times 16$ elements with the same side length of 0.025 m. The number of control points for the cable were kept at 6 for the quarter. Loads and prestressing force were also kept the same at $q = 2$ kN/m^2 and $T_{\text{pre}} = 2$ kN.

To account for the smaller domain, both the PDE filter radius r and cable-to-concrete filter radius r_{cf} were decreased to 0.05 m. The box constraints and move limits for the control points were subsequently also reduced to 0.05 m. The volume constraint was again set to $V^*_{int} = 0.3$ for both designs.

Give the large ratio difference, one would expect a significant geometrical variation, particularly the area under tension. But both beams in Figure 15 have nearly identical geometries, suggesting that the design constraints dominate over the objective functions.

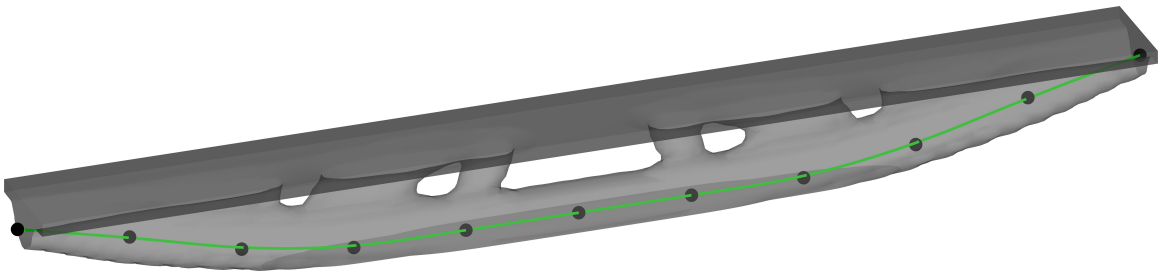

(a) $s_{ct} = 1$ (von Mises)

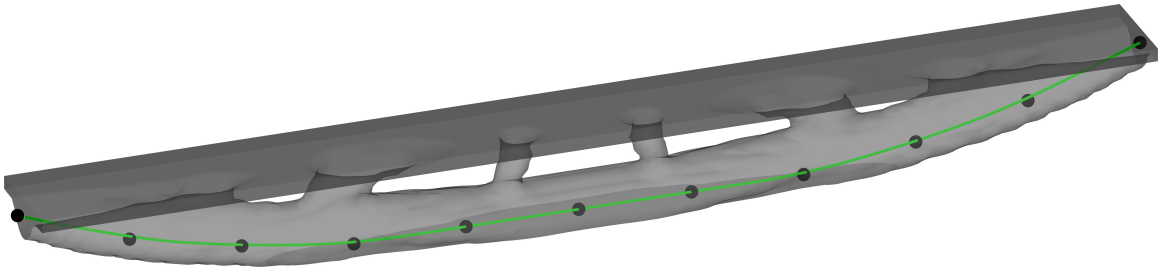

(b) $s_{ct} = 10$

Figure 15: Final design with different ratios of s_{ct}.

Cross-sectional slices in Figure 16 from the lengthwise midpoint reveal the internal structure size as well as the yield function values for the internal elements. Here, elements with a density over 0.5 are displayed. A beam under loading will be in compression at the top of the beam and in tension at the bottom. Both structures have similar yield values at the top of the structure due to the required 2 layer padding area for the force distribution.

The difference is apparent in the tension zone where, as expected, the structure with lower tensile strength had to compensate with more material. This resulted in a wider bottom part with stress levels close to the yield limit. This is in contrast to the von

Mises case where the size of the area in tension were determined by the PDE and cable-to-concrete filter radii rather than the yield limits.

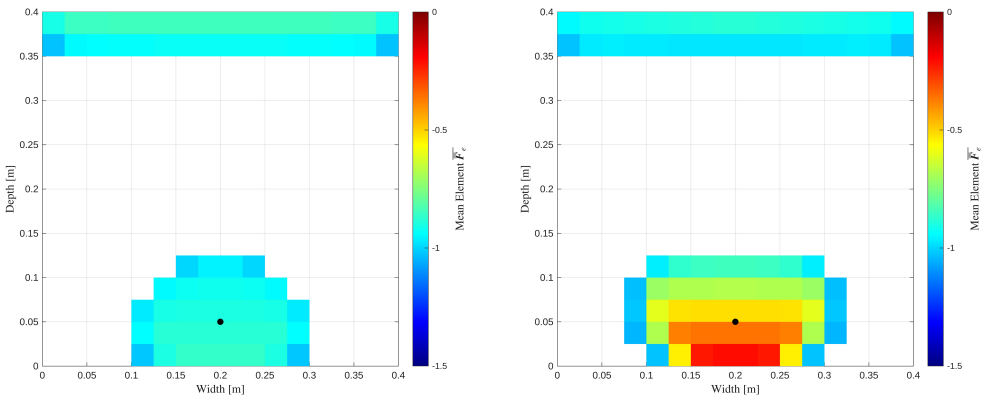

(a) $s_{ct} = 1$ (von Mises) (b) $s_{ct} = 10$

Figure 16: Lengthwise midpoint cross-sectional area with yield function values. Black dot represents cable placement.

The nearly identical density distributions and tendon layouts of the two beams resulted in comparable stiffness and structural responses, as quantified in Table 2.

Design	$\tilde{\phi}$ [-]	ϕ_1 [m^2]	ϕ_2 [kNm]	g_1 [m^3]	g_2 [-]	u_{sdp} [mm]	u_{l} [mm]
Initial	1.0000	0.0009	0.0012	0.1476	-0.3755 / 0.7489	-	-
$s_{ct} = 1$	0.2370	0.0001	0.0005	-0.0004	-0.5857	-1.0706	-0.0164
$s_{ct} = 10$	0.2459	0.0001	0.0005	-0.0003	-0.0601	-1.0803	-0.0169

Table 2: Function value comparisons between the initial design with the two runs of different stress limit ratios s_{ct}. The initial stress constraint function value was -0.3755 for $s_{ct} = 1$ and 0.7489 for $s_{ct} = 10$. Vertical displacements taken from the bottom midpoint.

7.3 Prestressing effect

The final example investigates the influence of the prestressing force T_{pre} in combination with the stress constraint. The geometry is identical to that of the previous example Section 7.2, and three otherwise identical load cases were analysed, differing only in the applied prestressing force. The load $q = 2$ kN/m^2 were kept the same and the yield limits were set to $\sigma_t = 5$ MPa and $s_{ct} = 5$. Yet again, the allowable volume fraction was $V^*_{int} = 0.3$.

Here after is (a) referred to the case without prestressing, (b) to $T_{\text{pre}} = 2$ kN and (c) to $T_{\text{pre}} = 4$ kN.

Figure 17 shows the final designs for the three cases with small differences between case (a) and (b) but significant variation in case (c).

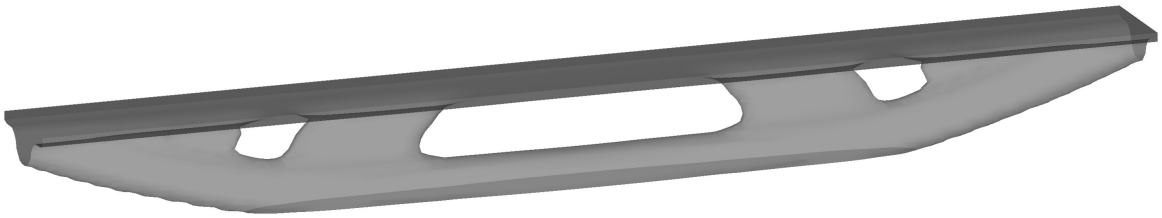

(a) $T_{\text{pre}} = 0$ kN

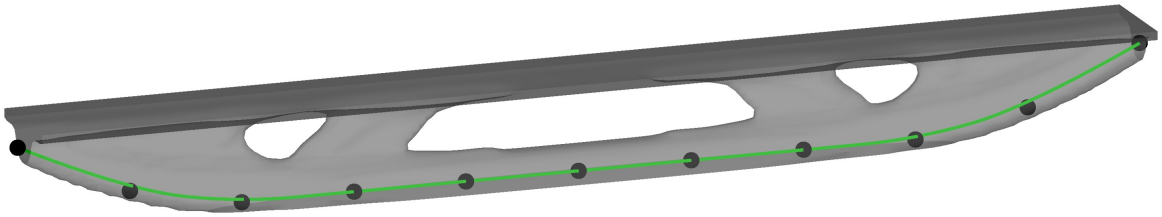

(b) $T_{\text{pre}} = 2$ kN

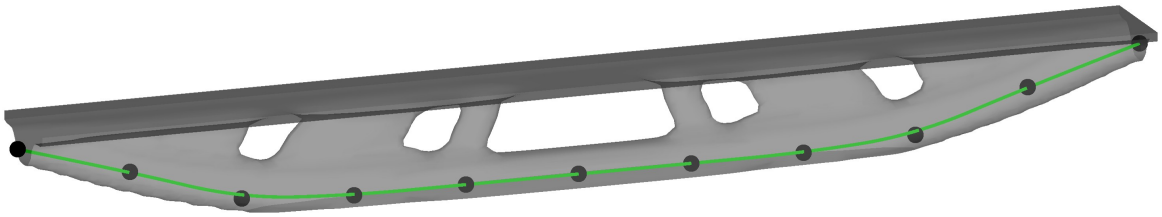

(c) $T_{\text{pre}} = 4$ kN

Figure 17: Final designs.

The middlepoint cross-sections in Figure 16 also shows little to no difference. As expected, the yield function value in the area under tension is slightly lower in the prestressed structures.

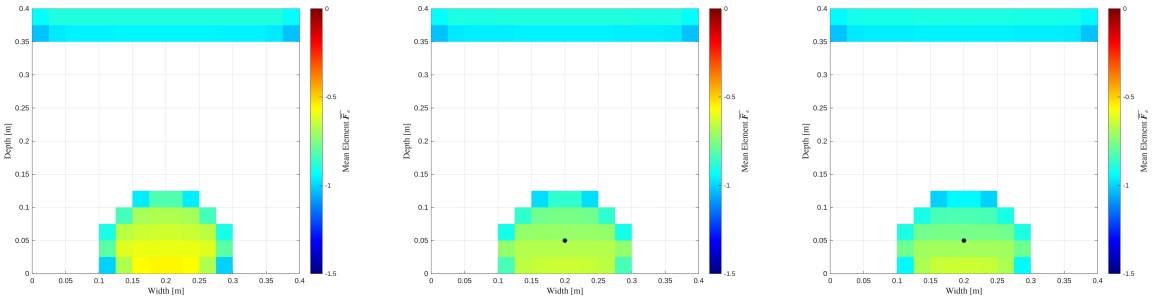

(a) $T_{\text{pre}} = 0$ kN (b) $T_{\text{pre}} = 2$ kN (c) $T_{\text{pre}} = 4$ kN

Figure 18: Lengthwise midpoint cross-sectional area with yield function values. Black dot represents cable placement.

Not surprisingly, case (b) performed better than case (a) with lower objective function value and less displacements by both permanent loads and the live load. Case (c) with higher prestressing didn't perform better than case (b). The displacement and

objective function values are comparable but case (b) had significantly lower maximum yield stress values as seen in Table 3. This can be explained using the fact that prestressing doesn't increase stiffness, but one would expect the absolute displacement due to permanent loads u_{sdp} to be lower in case (c) for all nodes in the structure. It should be noted that the displacement shown in the table here is not accounted for in the displacements used in the objective functions which is also why they are blanked out for the initial designs since the bottom layer does not have any material.

Design	$\tilde{\phi}$ [-]	ϕ_1 [m^2]	ϕ_2 [kNm]	g_1 [m^3]	g_2 [-]	u_{sdp} [mm]	u_{l} [mm]
Initial	1.0000	0.0010	0.0012	0.1476	0.0571	-	-
Final	0.2509	0.0001	0.0005	-0.0003	-0.3560	-0.4949	-0.3192

(a) $T_{\text{pre}} = 0$ kN

Design	$\tilde{\phi}$ [-]	ϕ_1 [m^2]	ϕ_2 [kNm]	g_1 [m^3]	g_2 [-]	u_{sdp} [mm]	u_{l} [mm]
Initial	1.0000	0.0009	0.0012	0.1476	-0.0095	-	-
Final	0.2078	0.0001	0.0004	-0.0003	-0.4643	-0.3795	-0.2724

(b) $T_{\text{pre}} = 2$ kN

Design	$\tilde{\phi}$ [-]	ϕ_1 [m^2]	ϕ_2 [kNm]	g_1 [m^3]	g_2 [-]	u_{sdp} [mm]	u_{l} [mm]
Initial	1.0000	0.0007	0.0012	0.1476	0.1809	-	-
Final	0.2244	0.0001	0.0004	-0.0003	-0.1196	-0.3761	-0.3752

(c) $T_{\text{pre}} = 4$ kN

Table 3: Function value comparisons for the three cases. Vertical displacements are from bottom-most midpoint.

8 Conclusions

This thesis successfully integrates a stress constraint into the existing framework for 3D optimization of prestressed concrete. The results confirm the validity and the framework now produces designs that comply with the mechanical limits of concrete. One finding is the expected trade-off between the objective function and the constraints. Introducing the stress constraint interacts with both the volume constraint and the objective function in a counteractive manner which increased the problem complexity. This sometimes leads to unstable convergence and cases where both constraints can't be fulfilled at the same time.

The Drucker-Prager criterion proved to be a suitable choice for this project, capturing the behavior of concrete under tension better than the von Mises model. While other newer and more advanced yield functions could potentially improve accuracy, Drucker-Prager remains an established and reliable method. Stress singularities were not observed and approximation errors introduced by the KS aggregation function were low and acceptable.

For the future, a refactoring of the anchoring force could be made to include some force dispersion device to potentially include higher prestressing forces. Computational optimization of the stress constraint could perhaps also be made which is desirable since the time complexity of an increased design domain scales exponentially. A future improvement may also consider buckling, eigenfrequency or manufacturability. Another aspect to consider is frictional losses and fatigue in the tendon.

References

[1] Martin (Engineer) Peck. *Concrete: Design, Construction, Examples*. Birkhäuser, 2006. ISBN: 9783038212966.

[2] Robbie M. Andrew. "Global CO2 emissions from cement production, 19282018". en. In: *Earth System Science Data* 11.4 (Nov. 2019), pp. 1675–1710. DOI: 10.5194/essd-11-1675-2019. URL: http://dx.doi.org/10.5194/essd-11-1675-2019.

[3] Ivar Björnsson et al. *Resursslöseri i anläggningsbyggandet?: Vad kan vi lära av 50 års utveckling?* svenska. TVBK 3080. Div. of Structural Engineering, Lund University, Feb. 2025. ISBN: 978-91-87993-28-2.

[4] Phoenix7777. *Post-Tensioned Concrete [SVG diagram]*. https://commons.wikimedia.org/wiki/File:Post-Tensioned_Concrete.svg. Licensed under CC BY-SA 4.0: https://creativecommons.org/licenses/by-sa/4.0/. Mar. 2018.

[5] Ticho Ooms et al. *The Production of a Topology-Optimized 3D-Printed Concrete Bridge*. en. 2022. DOI: 10.1007/978-3-031-06116-5_6. URL: http://dx.doi.org/10.1007/978-3-031-06116-5_6.

[6] Wenyu Lin et al. "Multi-scale fabrication and challenges in 3D printing of special -shaped concrete structures". en. In: *Journal of Building Engineering* 111 (Oct. 2025), p. 113134. DOI: 10.1016/j.jobe.2025.113134. URL: http://dx.doi.org/10.1016/j.jobe.2025.113134.

[7] Emad Shakur, Adaya Shaked, and Oded Amir. "Topology and shape optimization of 3D prestressed concrete structures". en. In: *Engineering Structures* 321 (Dec. 2024), p. 118936. DOI: 10.1016/j.engstruct.2024.118936. URL: http://dx.doi.org/10.1016/j.engstruct.2024.118936.

[8] Oded Amir and Emad Shakour. "Simultaneous shape and topology optimization of prestressed concrete beams". en. In: *Structural and Multidisciplinary Optimization* 57.5 (2018), pp. 1831–1843. DOI: 10.1007/s00158-017-1855-5. URL: http://dx.doi.org/10.1007/s00158-017-1855-5.

[9] Oded Amir and Emad Shakour. "Topology optimization of post-tensioned concrete beams". In: *Proceedings of IASS Annual Symposia, International Association for Shell and Spatial Structures* (19 2018), pp. 1–8.

[10] Zixin Zhang et al. "Isogeometric analysis-based design of post-tensioned concrete beam towards construction-oriented topology optimization". en. In: *Structural and Multidisciplinary Optimization* 64.6 (2021), pp. 4237–4253. DOI: 10.1007/s00158-021-03058-z. URL: http://dx.doi.org/10.1007/s00158-021-03058-z.

[11] Ishan Jha and Krishna K. Pathak. "Synergetic concrete shape and cable layout optimization of pre-stressed concrete beams". en. In: *Structural and Multidisciplinary Optimization* 66.4 (Mar. 2023). DOI: 10.1007/s00158-023-03545-5. URL: http://dx.doi.org/10.1007/s00158-023-03545-5.

[12] Niels Saabye Ottosen and Hans Petersson. *Introduction to the finite element method*. Prentice Hall, 1992. ISBN: 0134738772.

[13] O. Sigmund. “A 99 line topology optimization code written in Matlab”. en. In: *Structural and Multidisciplinary Optimization* 21.2 (Apr. 2001), pp. 120–127. DOI: 10.1007/s001580050176. URL: http://dx.doi.org/10.1007/s001580050176.

[14] Krister Svanberg. “The method of moving asymptotesa new method for structural optimization”. en. In: *International Journal for Numerical Methods in Engineering* 24.2 (Feb. 1987), pp. 359–373. DOI: 10.1002/nme.1620240207. URL: http://dx.doi.org/10.1002/nme.1620240207.

[15] A. Díaz and O. Sigmund. “Checkerboard patterns in layout optimization”. en. In: *Structural Optimization* 10.1 (Aug. 1995), pp. 40–45. DOI: 10.1007/bf01743693. URL: http://dx.doi.org/10.1007/bf01743693.

[16] B Bourdin. “Filters in topology optimization”. In: *INTERNATIONAL JOURNAL FOR NUMERICAL METHODS IN ENGINEERING* 50 (9 2001), pp. 2143–2158.

[17] B. S. Lazarov and O. Sigmund. “Filters in topology optimization based on Helmholtztype differential equations”. en. In: *International Journal for Numerical Methods in Engineering* 86.6 (Dec. 2010), pp. 765–781. DOI: 10.1002/nme.3072. URL: http://dx.doi.org/10.1002/nme.3072.

[18] Mathias Wallin et al. “Consistent boundary conditions for PDE filter regularization in topology optimization”. en. In: *Structural and Multidisciplinary Optimization* 62.3 (Apr. 2020), pp. 1299–1311. DOI: 10.1007/s00158-020-02556-w. URL: http://dx.doi.org/10.1007/s00158-020-02556-w.

[19] Ole Sigmund. “Morphology-based black and white filters for topology optimization”. en. In: *Structural and Multidisciplinary Optimization* 33.45 (Jan. 2007), pp. 401–424. DOI: 10.1007/s00158-006-0087-x. URL: http://dx.doi.org/10.1007/s00158-006-0087-x.

[20] Fengwen Wang, Boyan Stefanov Lazarov, and Ole Sigmund. “On projection methods, convergence and robust formulations in topology optimization”. en. In: *Structural and Multidisciplinary Optimization* 43.6 (Dec. 2010), pp. 767–784. DOI: 10.1007/s00158-010-0602-y. URL: http://dx.doi.org/10.1007/s00158-010-0602-y.

[21] M. P. Bendsøe and O. Sigmund. “Material interpolation schemes in topology optimization”. In: *Archive of Applied Mechanics (Ingenieur Archiv)* 69.910 (Nov. 1999), pp. 635–654. DOI: 10.1007/s004190050248. URL: http://dx.doi.org/10.1007/s004190050248.

[22] D. C. DRUCKER and W. PRAGER. “SOIL MECHANICS AND PLASTIC ANALYSIS OR LIMIT DESIGN”. In: *Quarterly of Applied Mathematics* 10.2 (1952), pp. 157–165. ISSN: 0033569X, 15524485. URL: http://www.jstor.org/stable/43633942 (visited on 07/28/2025).

[23] R. v. Mises. “Mechanik der festen Körper im plastisch- deformablen Zustand”. In: *Nachrichten von der Gesellschaft der Wissenschaften zu Göttingen, Mathematisch-Physikalische Klasse* 1913 (1913), pp. 582–592. URL: http://eudml.org/doc/58894.

[24] G. D. Cheng and X. Guo. "ϵ-relaxed approach in structural topology optimization". en. In: *Structural Optimization* 13.4 (1997), pp. 258–266. DOI: 10.1007/bf01197454. URL: http://dx.doi.org/10.1007/BF01197454.

[25] G. Kreisselmeier and R. Steinhauser. "Systematic Control Design by Optimizing a Vector Performance Index". en. In: *IFAC Proceedings Volumes* 12.7 (1979), pp. 113–117. DOI: 10.1016/s1474-6670(17)65584-8. URL: http://dx.doi.org/10.1016/s1474-6670(17)65584-8.